INTERNATIONAL JOURNAL FOR NUMERICAL METHODS IN FLUIDS
Int. J. Numer. Meth. Fluids 2000; **34**: 729–750

Finite element solution of three-dimensional turbulent flows applied to mold-filling problems

F. Ilinca*,[1] and J.-F. Hétu

Industrial Materials Institute, National Research Council of Canada 75, de Mortagne, Boucherville, Quebec, Canada J4B 6Y4

SUMMARY

This paper presents a finite element solution algorithm for three-dimensional isothermal turbulent flows for mold-filling applications. The problems of interest present unusual challenges for both the physical modelling and the solution algorithm. High-Reynolds number transient turbulent flows with free surfaces have to be computed on complex three-dimensional geometries. In this work, a segregated algorithm is used to solve the Navier–Stokes, turbulence and front-tracking equations. The streamline–upwind/Petrov–Galerkin method is used to obtain stable solutions to convection-dominated problems. Turbulence is modelled using either a one-equation turbulence model or the κ–ε two-equation model with wall functions. Turbulence equations are solved for the natural logarithm of the turbulence variables. The change of dependent variables allows for a robust solution algorithm and good predictions even on coarse meshes. This is very important in the case of large three-dimensional applications for which highly refined meshes result in untreatable large numbers of elements. The position of the flow front in the mold cavity is computed using a level set approach. Finally, equations are integrated in time using an implicit Euler scheme. The methodology presents the robustness and cost effectiveness needed to tackle complex industrial applications. Copyright © 2000 John Wiley & Sons, Ltd.

KEY WORDS: finite elements; logarithms; mold-filling; three-dimensional; turbulent flow

1. INTRODUCTION

Industrial mold-filling problems involve fluid flow coupled with free surfaces, non-constant material properties, and complicated three-dimensional geometries. The flow may be at a high Reynolds number or on geometries having high aspect ratio components. Strong non-linear dependence of flow properties on velocity are commonplace, such as large and rapid spatial variations of the eddy viscosity for turbulent flows. During the casting of complex industrial parts, the molten alloy flows through converging and diverging sections as well as in areas

* Correspondence to: Industrial Materials Institute, CNRC-NRC, 75, de Mortagne, Boucherville, Quebec, Canada J4B 6Y4. Tel.: + 1 450 6415365; fax: + 1 450 6415104.

[1] E-mail: florin.ilinca@nrc.ca

Received 7 September 1999
Revised 22 February 2000

Copyright © 2000 John Wiley & Sons, Ltd.

presenting drastic changes in thickness and flow directions. Typical examples of these cases include flow in ribs, short flow lengths, large transitions in cavity thickness, sudden contractions/expansions (gates), corners and channels with low aspect ratios. In many cases these regions can be the source of casting problems (air entrapment, porosity, etc.) and a more detailed understanding of the flow characteristics in these areas might be useful in solving undesirable situations. Such problems place special demands on the solution algorithm. The technique must be robust and provide accurate solutions for a wide range of parameters. This paper presents a finite element method capable of tackling these difficulties.

When using finite elements, the common choice is the standard Galerkin method. Therefore, the trial and interpolation functions are identical, which makes the method work best when the diffusion is important. However, if convection dominates spurious oscillations can occur in the numerical solution. Moreover, the Galerkin method involves limitations in the choice of velocity–pressure interpolants, which must satisfy the Babuška–Brezzi condition. In the last decade, stabilization methods, such as the streamline–upwind/Petrov–Galerkin (SUPG) and the Galerkin/least-squares (GLS), became more and more popular. Such methods solve convective-dominated problems by adding stabilization terms to the Galerkin formulation [1–3]. Moreover, SUPG and GLS methods allow the use of velocity and pressure interpolants that do not satisfy the Babuška–Brezzi condition [2]. This makes it possible to use linear equal-order interpolation functions, which are both computationally effective and easy to implement, especially for three-dimensional applications. Another critically important benefit of stabilized methods is that the underlying linear systems become amenable to non-symmetric preconditioned iterative solvers, suitable for large-scale three-dimensional problems [4].

Two-equation turbulence models are very popular for solving turbulent flows. They usually involve transport equations for the turbulence kinetic energy (TKE) and for a second turbulence variable in order to evaluate the eddy viscosity.

Two-equation models with wall functions have shown to be a powerful tool to solve complex turbulent flows because they provide good predictions at low computational cost [5–7]. One major hurdle in the numerical treatment of two-equation models lies in ensuring that the turbulence variables (here k and ϵ) remain positive throughout the flow domain and during the course of iterations. The same problem occurs when using one-equation turbulence models. Failure to ensure positivity can have devastating effects on the solution process. The eddy viscosity may locally become negative and result in immediate and irrecoverable breakdown of iterations. The current authors propose to use a change of dependent variables for turbulence quantities, which results in improved solution quality [8,9]. The computational variables are the natural logarithm of the original turbulence variables. This choice has several important advantages. Turbulence variables and source terms in the turbulence equations are now obtained as the exponential of the computational-dependent variables. Hence, these terms are all strictly positive throughout the domain. The change of variables also results in improved accuracy in regions of rapid variation of turbulence fields, such as boundary layers, stagnation points, and shear layers [9]. This behavior is mainly due to the fact that a linear interpolation of the logarithms is closer to the real solution that a linear interpolation of the turbulence variables themselves.

Copyright © 2000 John Wiley & Sons, Ltd.

The improvement in the solution accuracy is even more pronounced on coarse meshes [9]. This last advantage is very important in the case of large three-dimensional applications for which the mesh refinement generates a large increase in the size of the systems to be solved. As an example, a reduction by a factor of two in the size of the elements results in an eight-times increase in the number of elements. Often such refined meshes become too large to be solved in a reasonable amount of time. A unified solution algorithm for two-equation models of turbulence based on the use of logarithmic variables is presented in Reference [10]. Applications are shown for the standard $k-\epsilon$ model, the $k-\tau$ model of Speziale, and the $k-\omega$ model of Wilcox. The procedure is general and is applicable to all one- and two-equation models of turbulence.

In this work, turbulence is modeled by using the $k-\epsilon$ model of turbulence. A simple one-equation model based on the Prandtl mixing length hypothesis is also presented. The equations of both turbulence models are solved for the logarithms of turbulence variables. The position of the flow front in the mold cavity is computed using a level set approach. Integration in time is made using an implicit Euler scheme. Finally, at each time step, the system of equations (Navier–Stokes, turbulence and front-tracking equations) is solved in a segregated manner.

The paper is organized as follows. Section 2 presents the flow and front-tracking equations. Section 3 discusses the change of variables leading to the logarithmic form of the turbulence equations. Section 4 summarizes the finite element formulation. The solution algorithm is discussed in Section 5. Section 6 presents results obtained on mold-filling problems. The numerical solutions are compared with the experiments. Section 7 concludes the paper.

2. GOVERNING EQUATIONS

The solution method solves the Reynolds-averaged Navier–Stokes (RANS) and turbulence equations on a portion of the cavity, which at a given time is partly filled with fluid and partly filled with air. For each time step, the Navier–Stokes equations are solved only on elements which contain fluid (filled region of the cavity) or which can contain fluid on the next time step (transition zone), as determined by using the maximum flow velocity on the fluid–air interface. The velocity field in the fluid always satisfies a divergence-free condition. Consequently, flow front progression is not simply extrapolated from the normal velocity of the interface but is based on the incompressible flow field and convected accordingly. In the transition zone, the pressure is considered constant, equal, for example, to the atmospheric pressure. Therefore, for entirely unfilled elements, the pressure gradient and the continuity equation are dropped from the mathematical model. That makes the air in the transition zone behave like an infinitely compressible fluid. Another choice in this implementation is to consider the air in the transition zone inertialess. Being inertialess, the air will respond instantaneously to the constraints imposed by the liquid progression. This overcomes the problem of computing undefined time derivatives in the transition zone.

Copyright © 2000 John Wiley & Sons, Ltd.

2.1. Reynolds-averaged Navier–Stokes equations

The flow regime of interest is modeled by the incompressible RANS equations

$$\rho\left(\frac{\partial \mathbf{u}}{\partial t}+\mathbf{u}\cdot\nabla\mathbf{u}\right)=-\nabla p+\nabla\cdot[2(\mu+\mu_T)\dot{\gamma}(\mathbf{u})]+\rho\mathbf{g} \tag{1}$$

$$\nabla\cdot\mathbf{u}=0 \tag{2}$$

where $\dot{\gamma}(\mathbf{u})=(\nabla\mathbf{u}+\nabla\mathbf{u}^T)/2$ is the strain rate tensor, ρ is the density, μ is the fluid viscosity, and $\mathbf{g}$ is the gravity force. The properties (density and fluid viscosity) depend on a *level set* function F denoting the interface position. For example, density in a filled element has the value ρ_l, and in an unfilled element the value ρ_g (here $\rho_g=0$), and for partly filled elements is interpolated between those two values based on the volumetric fraction.

Boundary conditions imposed on the Navier–Stokes equations are

$$\mathbf{u}=\mathbf{u}_i \quad \text{or} \quad 2(\mu+\mu_\mathrm{T})\dot{\gamma}(\mathbf{u})\cdot\mathbf{n}-p\mathbf{n}=\boldsymbol{\tau}_i \quad \text{on } \Gamma_\text{inlet}$$

$$\left.\begin{array}{l} 2(\mu+\mu_\mathrm{T})\dot{\gamma}(\mathbf{u})\cdot\mathbf{n}-p\mathbf{n}=\boldsymbol{\tau}_\mathrm{w} \\ \mathbf{u}\cdot\mathbf{n}=0 \end{array}\right\} \quad \text{on } \Gamma_\text{wall} \tag{3}$$

The turbulent viscosity μ_T is computed using either a one-equation turbulence model or the two-equation k–ϵ model. The system is closed by including the transport equations for turbulence quantities.

2.2. The one-equation model

The one-equation turbulence model used here solves a transport equation for the turbulence kinetic energy k [11]

$$\rho\left(\frac{\partial k}{\partial t}+\mathbf{u}\cdot\nabla k\right)=\nabla\cdot\left[\left(\mu+\frac{\mu_\mathrm{T}}{\sigma_k}\right)\nabla k\right]+\mu_\mathrm{T}P(\mathbf{u})-\rho\epsilon \tag{4}$$

where σ_k is a constant ($\sigma_k=1.0$) and the production of turbulence is defined as

$$P(\mathbf{u})=\nabla\mathbf{u}:\ (\nabla\mathbf{u}+\nabla\mathbf{u}^T) \tag{5}$$

The TKE dissipation, ϵ, is computed from the turbulence kinetic energy and the mixing length, l_m, as

$$\epsilon=\frac{C_\mu^{3/4}k^{3/2}}{l_\mathrm{m}} \tag{6}$$

where C_μ is a constant taken as 0.09. Finally, the eddy viscosity is computed from k and l_m by

Copyright © 2000 John Wiley & Sons, Ltd.

$$\mu_{\mathrm{T}} = \rho C_{\mu}^{1/4} k^{1/2} l_{\mathrm{m}} \tag{7}$$

In the present approach, we consider that the mixing length is given by $l_{\mathrm{m}} = \kappa y$ [12], where κ is the von Karman constant, $\kappa = 0.4$, and y is the distance to the nearest wall.

2.3. The standard k–ϵ model

For this model, the turbulence quantities are the turbulence kinetic energy k and its dissipation rate ϵ. Hence, an additional transport equation for ϵ must be solved [11]

$$\rho\left(\frac{\partial \epsilon}{\partial t} + \mathbf{u}\cdot\nabla\epsilon\right) = \nabla\cdot\left[\left(\mu + \frac{\mu_{\mathrm{T}}}{\sigma_{\epsilon}}\right)\nabla\epsilon\right] + C_{\epsilon l}\frac{\epsilon}{k}\mu_{\mathrm{T}}P(\mathbf{u}) - C_{\epsilon 2}\rho\frac{\epsilon^2}{k}$$

The eddy viscosity is computed from k and ϵ by

$$\mu_{\mathrm{T}} = \rho C_{\mu}\frac{k^2}{\epsilon} \tag{8}$$

The constants σ_k, σ_{ϵ}, $C_{\epsilon 1}$, $C_{\epsilon 2}$, C_{μ} take on the standard values [11]

$$\sigma_k = 1.0, \quad \sigma_{\epsilon} = 1.3, \quad C_{\epsilon 1} = 1.44, \quad C_{\epsilon 2} = 1.92, \quad C_{\mu} = 0.09$$

2.4. Wall boundary conditions

On the boundaries, a combination of Neumann (tangential) and Dirichlet (normal) conditions are imposed using wall functions. These describe the asymptotic behavior of the different variables near a solid wall [11]. The velocity is constrained to be tangent to the wall by imposing the normal velocity to zero. This tangency condition is imposed in a nodal fashion. Following Engelman *et al.* [13], the normal direction is computed for each node on the surface such that the global mass flux across the boundary is zero. When using continuous piecewise linear velocities, computation of the nodal normal direction at node i reduces to

$$n_{x_i} = \frac{1}{n_i}\sum_{e_i} A^{(e_i)} n_x^{(e_i)}, \qquad n_{y_i} = \frac{1}{n_i}\sum_{e_i} A^{(e_i)} n_y^{(e_i)}, \qquad n_{z_i} = \frac{1}{n_i}\sum_{e_i} A^{(e_i)} n_z^{(e_i)} \tag{9}$$

where

$$n_i = \left[\left(\sum_{e_i} A^{(e_i)} n_x^{(e_i)}\right)^2 + \left(\sum_{e_i} A^{(e_i)} n_x^{(e_i)}\right)^2 + \left(\sum_{e_i} A^{(e_i)} n_x^{(e_i)}\right)^2\right]^{1/2} \tag{10}$$

In the above equations, e_i denotes the boundary elements containing the node i, $A^{(e_i)}$ is the surface of the boundary element e_i, and $n_x^{(e_i)}$, $n_y^{(e_i)}$, $n_z^{(e_i)}$ represent the Cartesian components of the unit vector, nomal to element e_i.

The wall shear stress given by the law of the wall is imposed on two orthogonal tangential directions defining the tangency plane. The present procedure deals with arbitrary three-dimensional geometries, and the solution approach is adapted to cases for which the normal and tangential directions do not correspond to the Cartesian co-ordinates. We use a simple yet efficient approach, which needs no change of co-ordinates between the Cartesian system and the local normal–tangential system. Let us note the momentum equation residual as a vector **R** (the solution is obtained for $\mathbf{R} = 0$) for which the Cartesian components are noted R_x, R_y, and R_z

$$\mathbf{R} = R_x\hat{\mathbf{i}} + R_y\hat{\mathbf{j}} + R_z\hat{\mathbf{k}} = 0 \tag{11}$$

Here $\hat{\mathbf{i}}$, $\hat{\mathbf{j}}$, and $\hat{\mathbf{k}}$ are unit vectors in the Cartesian frame of reference. The momentum equation in a given direction, $\mathbf{a} = a_x\hat{\mathbf{i}} + a_y\hat{\mathbf{j}} + a_z\hat{\mathbf{k}}$, is obtained directly by projecting the residual vector **R** onto that direction [13]

$$R_a = \mathbf{R}\cdot\mathbf{a} = R_x a_x + R_y a_y + R_z a_z = 0 \tag{12}$$

This applies to both the system of partial differential equations and its variational form. Therefore, the finite element equations corresponding to the two tangential directions $\hat{\mathbf{t}}_1$ and $\hat{\mathbf{t}}_2$ are simply obtained as

$$R_{t_1} = \mathbf{R}\cdot\hat{\mathbf{t}}_1 = R_x t_{x1} + R_y t_{y1} + R_z t_{z1} = 0 \tag{13}$$

$$R_{t_2} = \mathbf{R}\cdot\hat{\mathbf{t}}_2 = R_x t_{x2} + R_y t_{y2} + R_z t_{z2} = 0 \tag{14}$$

and we remark that the unknowns remain the Cartesian components of the velocity and no change of co-ordinates in needed. Equations in tangential directions are just linear combinations of the equations in Cartesian co-ordinates. The third nodal equation constrains the normal velocity to be zero

$$\mathbf{u}\cdot\hat{\mathbf{n}} = un_x + vn_y + wn_z = 0 \tag{15}$$

where n_x, n_y, and n_z are the Cartesian components of the nodal unit normal vector $\hat{\mathbf{n}}$.

It remains to determine the value of the wall shear stress, which is given by the law of the wall

$$\tau_{\mathrm{w}} = -\frac{\rho C_\mu^{1/4} k_{\mathrm{w}}^{1/2}}{U^+}\mathbf{u}_{\mathrm{t}} \tag{16}$$

where

$$U^+ = \begin{cases} y^+, & y^+ < y_c^+ \\ \dfrac{1}{\kappa}\ln(Ey^+), & y^+ \geq y_c^+ \end{cases} \tag{17}$$

Copyright © 2000 John Wiley & Sons, Ltd.

$$y^+ = \frac{\rho C_\mu^{1/4} k_w^{1/2} y}{\mu} \tag{18}$$

Here $\mathbf{u}_t$ is the tangential velocity ($\mathbf{u}_t = (\mathbf{u}\cdot\hat{\mathbf{t}}_1)\hat{\mathbf{t}}_1$ for the first tangential direction and $\mathbf{u}_t = (\mathbf{u}\cdot\hat{\mathbf{t}}_2)\hat{\mathbf{t}}_2$ for the second one), y is the distance between the computational boundary and the wall, κ is the von Karman constant and E is a roughness parameter ($E = 9.0$ for smooth walls). Equation (16) indicates that the shear stress acts in the opposite direction of that of the tangential velocity. The TKE values at boundary points k_w are computed implicitly by setting the normal derivative of the TKE to zero at the wall. Finally, for the k–ϵ model, the TKE dissipation rate on boundary points is obtained by using

$$\epsilon_w = \frac{C_\mu^{3/4} k_w^{3/2}}{\kappa y} \tag{19}$$

2.5. Front-tracking equation

The position of the flow front in the cavity is modeled using a level set method [14,15]. This approach defines a smooth function $F(\mathbf{x}, t)$ such that a critical value F_c represents the position of the free surface. The function $F(\mathbf{x}, t)$ is defined as

$$F(\mathbf{x}, t) = \begin{cases} F_c + d(\mathbf{x}, t), & \mathbf{x} \text{ in filled region} \\ F_c, & \mathbf{x} \text{ on the interface} \\ F_c - d(\mathbf{x}, t), & \mathbf{x} \text{ in empty region} \end{cases} \tag{20}$$

where $d(\mathbf{x})$ represents the distance from the interface [16]. Initial values $F(\mathbf{x}, t = 0)$ are given to define the initial position of the flow front. The pseudo-concentration function is convected using the velocity field provided by the solution of the Navier–Stokes equations

$$\frac{\partial F}{\partial t} + \mathbf{u}\cdot\nabla F = 0 \quad \text{on } \Omega \tag{21}$$

The function F is reinitialized after each time step to insure mass conservation of the liquid phase. The mass correction procedure is as follows:

1. Locate the free surface and reinitialize F using Equation (20).
2. Compute the theoretical volume filled V_{theo} from the volume filled at the previous time step V_{f0} and the volumetric flux entering the domain, $V_{\text{theo}} = V_{f0} + \Delta t \int_{\Gamma_{\text{inlet}}} |\mathbf{u}\cdot\hat{\mathbf{n}}| \, ds$.
3. Find F^* such that $V_{\text{theo}} = V_f(F^*)$, with $V_f(F^*)$ representing the volume of the cavity where $F(x) > F^*$. The surface $F(x) = F^*$ represents the mass conserving free surface.
4. Modify F in order to translate the corrected interface from F^* to F_c: $F(x) = F(x) - F^* + F_c$.

Copyright © 2000 John Wiley & Sons, Ltd.

3. LOGARITHMIC FORM OF THE TURBULENCE EQUATIONS

While mathematically correct, the turbulence equations in the previous section may lead to difficulties in the numerical solution algorithm. For example, the eddy viscosity may become negative in some cases if one of the turbulence variables becomes negative. This will cause a dramatic breakdown of the solution algorithm. Also, several source terms contain division by the value of one turbulence variable (k for example). Negative or small values of the denominator can lead to an improper sign or overly large values for μ_T or for some source terms. Enhanced robustness of the algorithm is achieved if one can ensure that turbulence variables remain positive throughout the domain and during the course of iterations.

One way to preserve positivity of the dependent variables consists of solving for their logarithms [8,9]. This can be viewed as using the following change of dependent variables:

$$\mathscr{K} = \ln(k), \qquad \mathscr{E} = \ln(\epsilon) \tag{22}$$

Solving for $\mathscr{K}$ and $\mathscr{E}$ guarantees that k and ϵ will remain positive throughout the computations. Hence, the eddy viscosity μ_T will always remain positive. This approach offers other advantages. Turbulence quantities most often present very steep fronts, which are difficult to resolve accurately. The fields of the logarithmic variables $\mathscr{K}$ and $\mathscr{E}$ present smoother variations than those of k and ϵ because the logarithm varies more slowly than its arguments. Hence, more accurate solutions are obtained when logarithmic variables are used [9]. A detailed comparison of the traditional solution procedure using k and ϵ as dependent variables and that solving for the logarithms may be found in References [9,10].

The equation for $\mathscr{K}$ is obtained by first dividing the k-equation by k, and by nothing that the gradient of $\mathscr{K}$ is equal to the gradient of k divided by k ($\nabla\mathscr{K} = (\nabla k)/k$). The $\mathscr{E}$-equation is obtained by a similar transformation. The turbulence equations and the eddy viscosity definition for logarithmic variables are then as follows:

one-equation model

$$\rho\left(\frac{\partial \mathscr{K}}{\partial t} + \mathbf{u}_{\mathscr{K}}\cdot\nabla\mathscr{K}\right) = \nabla\cdot\left[\left(\mu + \frac{\mu_T}{\sigma_k}\right)\nabla\mathscr{K}\right] + \rho C_\mu^{1/4}\,\mathrm{e}^{-\mathscr{K}/2} l_m P(\mathbf{u}) - \frac{\rho C_\mu^{3/4}}{l_m}\,\mathrm{e}^{\mathscr{K}/2} \tag{23}$$

$$\mu_T = \rho C_\mu^{1/4}\,\mathrm{e}^{\mathscr{K}/2} l_m \tag{24}$$

k–ϵ model

$$\rho\left(\frac{\partial \mathscr{K}}{\partial t} + \mathbf{u}_{\mathscr{K}}\cdot\nabla\mathscr{K}\right) = \nabla\cdot\left[\left(\mu + \frac{\mu_T}{\sigma_k}\right)\nabla\mathscr{K}\right] + \mu_T\,\mathrm{e}^{-\mathscr{K}} P(\mathbf{u}) - \rho\,\mathrm{e}^{\mathscr{E}-\mathscr{K}} \tag{25}$$

$$\rho\left(\frac{\partial \mathscr{E}}{\partial t} + \mathbf{u}_{\mathscr{E}}\cdot\nabla\mathscr{E}\right) = \nabla\cdot\left[\left(\mu + \frac{\mu_T}{\sigma_\epsilon}\right)\nabla\mathscr{E}\right] + C_{\epsilon1}\mu_T\,\mathrm{e}^{-\mathscr{K}} P(\mathbf{u}) - C_{\epsilon2}\rho\,\mathrm{e}^{\mathscr{E}-\mathscr{K}} \tag{26}$$

$$\mu_T = \rho C_\mu\,\mathrm{e}^{2\mathscr{K}-\mathscr{E}} \tag{27}$$

Copyright © 2000 John Wiley & Sons, Ltd.

The modified velocities $\mathbf{u}_{\mathscr{K}}$ and $\mathbf{u}_{\mathscr{E}}$ are defined as

$$\mathbf{u}_{\mathscr{K}} = \mathbf{u} - \frac{1}{\rho}\left(\mu + \frac{\mu_{\mathrm{T}}}{\sigma_k}\right)\nabla\mathscr{K} \tag{28}$$

$$\mathbf{u}_{\mathscr{E}} = \mathbf{u} - \frac{1}{\rho}\left(\mu + \frac{\mu_{\mathrm{T}}}{\sigma_\epsilon}\right)\nabla\mathscr{E} \tag{29}$$

Note that the equations for logarithmic variables are equivalent to the original equations of the turbulence models. Hence, there is no change in the turbulence models. The only modification is that the computational variables are now the logarithms of the turbulence quantities. The use of logarithmic variables has removed the potentially troublesome divisions by k and ϵ. Finally, a number of other worrisome divisions have been removed from the transport equations. The price to pay for this advantage is the appearance of exponentials in the right-hand side of the turbulence equations. However, since k and ϵ take on small values, the exponential is very flat so that the non-linearities are mild. In fact, our experience indicates that the use of logarithmic variables significantly enhances convergence of the solver.

4. VARIATIONAL FORMULATION

The incompressible Navier–Stokes and turbulence equations in the cavity are solved by a SUPG formulation [2,3,17]. Stabilization methods such as SUPG and GLS are built by adding stabilization terms to the Galerkin formulation. The Galerkin part of the variational equations is obtained by multiplying equations (1) by appropriate test functions and integrating over the domain of interest. Weak terms are then obtained by using the divergence theorem applied to the momentum diffusion and pressure gradient terms. The SUPG method contains additional stabilization terms that are integrated only on the element interiors. These terms provide smooth solutions to convection-dominated flows and deal with the velocity–pressure coupling so that equal-order interpolation results in a stable numerical scheme [2,3,17]. This makes it possible to use elements that do not satisfy the Babuška–Brezzi condition as is the case of the linear $P1$–$P1$ element [2,18]. SUPG also stabilizes the resulting linear systems, making them amenable for robust iterative solution. This last advantage is of critical importance for large-scale applications. For the Navier–Stokes equations and the linear elements used here, SUPG and GLS methods are identical.

The SUPG variational formulation of the momentum–continuity equations is [17]

$$\begin{aligned}
&\int_\Omega \left(\rho\frac{\partial\mathbf{u}}{\partial t} + \rho\mathbf{u}\cdot\nabla\mathbf{u} - \rho\mathbf{g}\right)\mathbf{v}\,\mathrm{d}\Omega + \int_\Omega 2(\mu + \mu_{\mathrm{T}})\dot{\gamma}(\mathbf{u}):\ \dot{\gamma}(\mathbf{v})\,\mathrm{d}\Omega - \int_\Omega p\nabla\cdot\mathbf{v}\,\mathrm{d}\Omega + \int_\Omega \nabla\cdot\mathbf{u}q\,\mathrm{d}\Omega\\
&+\sum_K \int_{\Omega_K}\left\{\rho\frac{\partial\mathbf{u}}{\partial t} + \rho\mathbf{u}\cdot\nabla\mathbf{u} + \nabla p - \nabla\cdot[2(\mu + \mu_{\mathrm{T}})\dot{\gamma}(\mathbf{u})] - p\mathbf{g}\right\}\cdot\tau_u\{\rho\mathbf{u}\cdot\nabla\mathbf{v} + \nabla q\}\,\mathrm{d}\Omega_K\\
&+\sum_K \int_{\Omega_K} \nabla\cdot\mathbf{u}\delta\nabla\cdot\mathbf{v}\,\mathrm{d}\Omega_K = 0
\end{aligned} \tag{30}$$

The integrals over the entire domain identify the Galerkin method, while the stabilization terms are integrated only on the element interiors. The stabilization parameters τ_u and δ are defined as [19,20]

$$\tau_u = \left[\left(\frac{2\rho}{\Delta t}\right)^2 + \left(\frac{2\rho|\mathbf{u}|}{h_K}\right)^2 + \left(\frac{4(\mu+\mu_T)}{m_k h_K^2}\right)^2\right]^{-1/2} \tag{31}$$

$$\delta = \frac{h_K^2}{2\tau_u} \tag{32}$$

Here h_K is the size of the element K. For linear elements, the coefficient m_k is set to 1/3 (see References [17,18]).

The same procedure is applied to the logarithmic form of the turbulence equations and to the front-tracking equation. For example, the $\mathscr{K}$-equation of the one-equation model results in

$$\int_\Omega \left(\rho\frac{\partial \mathscr{K}}{\partial t} + \rho\mathbf{u}_{\mathscr{K}}\cdot\nabla\mathscr{K} - \rho C_\mu^{1/4}\,\mathrm{e}^{-\mathscr{K}/2} l_\mathrm{m} P(\mathbf{u}) + \frac{\rho C_\mu^{3/4}}{l_\mathrm{m}}\,\mathrm{e}^{\mathscr{K}/2}\right) w\,\mathrm{d}\Omega + \int_\Omega \left(\mu + \frac{\mu_\mathrm{T}}{\sigma_k}\right)\nabla\mathscr{K}\cdot\nabla w\,\mathrm{d}\Omega$$
$$+ \sum_K \int_{\Omega_K} \left\{\rho\frac{\partial\mathscr{K}}{\partial t} + \rho\mathbf{u}_{\mathscr{K}}\cdot\nabla\mathscr{K} - \nabla\cdot\left[\left(\mu + \frac{\mu_\mathrm{T}}{\sigma_k}\right)\nabla\mathscr{K}\right] - \rho C_\mu^{1/4}\,\mathrm{e}^{-\mathscr{K}/2} l_\mathrm{m} P(\mathbf{u}) + \frac{\rho C_\mu^{3/4}}{l_\mathrm{m}}\,\mathrm{e}^{\mathscr{K}/2}\right\}$$
$$\cdot\,\tau_{\mathscr{K}}(\rho\mathbf{u}_{\mathscr{K}}\cdot\nabla w)\,\mathrm{d}\Omega_K = 0 \tag{33}$$

where

$$\tau_{\mathscr{K}} = \left[\left(\frac{2\rho}{\Delta t}\right)^2 + \left(\frac{2\rho|\mathbf{u}_{\mathscr{K}}|}{h_K}\right)^2 + \left(\frac{4(\mu+\mu_\mathrm{T}/\sigma_k)}{m_k h_K^2}\right)^2\right]^{-1/2} \tag{34}$$

Similar variational formulations are obtained for the k–ϵ model equations and for the front-tracking equation.

The momentum and continuity equations are solved using a mixed velocity–pressure formulation with $P1$–$P1$ tetrahedral elements. Scalar variables (logarithms of turbulence variables and front-tracking function) are discretized using piecewise linear continuous interpolants. Time is discretized with an implicit first-order Euler scheme. It means that all terms except the transient one are using the present time step values, while the time derivative term is discretized as

$$\frac{\partial u}{\partial t} = \frac{u - u_0}{\Delta t} \tag{35}$$

Here u is the present time step velocity and u_0 is the velocity at the previous time step. The same time integration scheme is used for all variables. From the authors' experience, even if such a method is more dissipative, it provides the needed robustness to deal with complex three-dimensional problems. A two-step, second-order scheme, such as the Gear scheme, while less dissipative, generates oscillations in regions of sharp gradients and needs small time steps to effectively improve the solution. The one-step second-order Runge–Kutta method is even less dissipative than the Gear scheme, and therefore is more sensitive to the presence of sharp gradients, as in near corners, in the wakes, and boundary layers. Moreover, this method provides the half-step solution for the pressure. Mass conservation, tangency conditions, and wall shear stress also correspond to the half-step solution. This fact may introduce additional errors that are difficult to estimate.

In order to control time integration errors, the present work uses a variable time step approach. Because during the filling process the solution changes mostly near the flow front, we impose a limit on the maximum Courant–Friedrichs–Lewy (CFL) number of elements located on the flow front

$$\Delta t = \min_{e \in \text{flow front}} \left(\frac{\text{CFL}_{\text{max}} L_e}{U_e} \right) \tag{36}$$

Here, U_e is the mean element velocity, L_e is the element size in the direction of the velocity, and CFL_{max} is the upper limit of the CFL number on elements located on the free surface.

5. SOLUTION ALGORITHM

The global system of equations is solved in a partly segregated manner. The solution algorithm is illustrated in Figure 1. At each time step, global iterates are performed for the momentum–

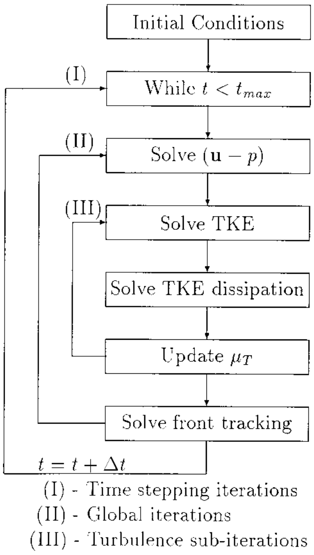

Figure 1. Solution algorithm.

Copyright © 2000 John Wiley & Sons, Ltd.

continuity, turbulence, and front-tracking equations. Sub-iterations of turbulence transport equations are also used to accelerate the overall convergence of the iterative process.

In References [9,21] a robust finite element scheme is obtained for the $k-\epsilon$ model by rewriting the equations for k and ϵ in block triangular form using the eddy viscosity definition. The current algorithm was modified in order to improve robustness and convergence. The logarithmic form of the turbulence equations implemented in the finite element algorithm is as follows:

$$\rho\left(\frac{\partial \mathscr{K}}{\partial t}+\mathbf{u}_{\mathscr{K}}\cdot\nabla\mathscr{K}\right)=\nabla\cdot\left[\left(\mu+\frac{\mu_{\mathrm{T}_i}}{\sigma_k}\right)\nabla\mathscr{K}\right]+\rho C_\mu^{1/4}\,\mathrm{e}^{-\mathscr{K}/2}l_{\mathrm{m}_i}P(\mathbf{u})-\frac{\rho C_\mu^{3/4}}{l_{\mathrm{m}_i}}\,\mathrm{e}^{\mathscr{K}/2} \tag{37}$$

$$\rho\left(\frac{\partial \mathscr{E}}{\partial t}+\mathbf{u}_{\mathscr{E}}\cdot\nabla\mathscr{E}\right)=\nabla\cdot\left[\left(\mu+\frac{\mu_{\mathrm{T}_i}}{\sigma_\epsilon}\right)\nabla\mathscr{E}\right]+\rho C_\mu C_{\epsilon 1}\,\mathrm{e}^{\mathscr{K}-\mathscr{E}}P(\mathbf{u})-\rho C_{\epsilon 2}\,\mathrm{e}^{\mathscr{E}-\mathscr{K}} \tag{38}$$

Subscript i indicates that the variable is computed using the solution from the previous iteration. As in Reference [9], the diffusion term, as well as the modified velocities $\mathbf{u}_{\mathscr{K}}$ and $\mathbf{u}_{\mathscr{E}}$, is computed using the eddy viscosity from the previous iteration, $\mu_{\mathrm{T}_i}=\rho C_\mu\,\mathrm{e}^{2\mathscr{K}_i-\mathscr{E}_i}$. However, the source terms were rewritten considering the equilibrium between turbulence variables throughout the mixing length

$$l_{\mathrm{m}}=C_\mu^{3/4}\,\mathrm{e}^{3/2\mathscr{K}-\mathscr{E}} \tag{39}$$

The $\mathscr{K}$-equation is solved as for the one-equation model using the mixing length computed from the previous iteration solution, $l_{\mathrm{m}_i}=C_\mu^{3/4}\,\mathrm{e}^{3/2\mathscr{K}_i-\mathscr{E}_i}$. Then, the $\mathscr{E}$-equation uses the last computed values for $\mathscr{K}$, and an implicit discretization for $\mathscr{E}$. This choice provides the right increment for $\mathscr{K}$ and maintains $\mathscr{K}$ and $\mathscr{E}$ in equilibrium.

The non-linear equations for the velocity and pressure are solved with a few Picard steps followed by Newton–Raphson iterations. For scalar equations, only Newton's iterations are performed. The resulting linear systems are generated directly in a compressed sparse row format [22], and solved using the biconjugate gradient stabilized (Bi-CGSTAB) iterative method [23] with an ILU preconditioner. An important reason for using the SUPG formulation is that it also stabilizes the linear systems, making them tractable by iterative solvers [4].

6. NUMERICAL RESULTS

The present solution approach is used to solve two three-dimensional isothermal turbulent mold-filling problems. The test cases presented are the filling of a plate and the gravity filling of a mold.

6.1. Filling of a plate

This problem was the subject of an experimental and numerical investigation by Schmid and Klein [24,25]. The plate is 150 mm high, 100 mm wide, and 2 mm thick. The gate has a width

Copyright © 2000 John Wiley & Sons, Ltd.

Table I. Computational characteristics for the flat plate.

Mesh	Number of nodes	Number of elements	Memory (Mb/processor)	Computational time
1	2052	6300	1	0:48 h
2	7881	25 200	5	6:40 h
3	30 879	100 800	17	53:00 h

of 45 mm. The cavity is filled with water. A kinematic viscosity of $\mu/\rho = 10^{-6}$ m^2 s^{-1} is used. The fluid enters the cavity at 16 m s^{-1} and the resulting Reynolds number based on the plate height is 2.4×10^6. Two-dimensional numerical simulations were performed by Schmid and Klein [24,25]. They considered a constant eddy viscosity, 20 times higher than the fluid viscosity. In the present case, computations use the k–ϵ turbulence model on three-dimensional meshes. Solutions were obtained for three different meshes. Computations were done on an Origin 2000 using four processors MIPS R10000 at 195 MHz, working in parallel. Mesh characteristics, memory requirements, and computational times are summarized in Table I. The flow front predictions are compared in Figure 2. The present prediction is close to the numerical solution of Schmid and Klein [24,25]. As expected, the free surface representation depends on the element size. However, there are little differences between the solutions on meshes 2 and 3. Numerical predictions for mesh 3 are compared with the experimental data in Figures 3 and 4. As can be seen, the agreement is good. Except for the interface instability, which cannot be reproduced in our numerical simulation, the filling features are well recovered. Some differences between the simulation and the experiment, especially at the end of the simulation, may be explained by the fact that the solution procedure considers the air infinitely compressible, as if it can exit freely from the cavity. In the experiment it cannot exit from the cavity. The simulation of the compressible fluid flow of the air in an enclosed cavity with a variable volume was not the objective of this work.

6.2. Gravity filling of a mold

For this application, the solutions obtained with the one-equation model and with the k–ϵ model are compared with the experiment performed by McLeod [26]. The fluid is a 50 per cent water/glycerine solution. This choice was made in order to recover fluid properties close to that of the liquid aluminum. The properties are summarized in Table II. In the experiment, the liquid flows from a 0.99-m height. However, a constant flow rate was experimentally observed by McLeod [26]. Hence, a constant inlet velocity of 0.216 m s^{-1} was used in the simulations. The gate laminar Reynolds number is about 10^4. The problem was solved for a dimensionless form of the equations. The reference length was considered as $L_0 = 2.54 \times 10^{-2}$ m and the reference velocity was compute from $U_0 = \sqrt{gL_0} = 0.5$ m s^{-1}, where $g = 9.81$ m s^{-2} is gravity. This results in a dimensionless gravity equal to unity. The gravity acts on the vertical plane from up to down. The reference pressure is given by $p_0 = \rho g L_0 = 280$ N m^{-2}.

The simulation time runs from 0 to 6.5 s in variable time steps. The time step was computed in order to obtain a maximum CFL number equal to 0.7 on the fluid–air interface. A total of 600 time steps were required to complete the simulation. For each time step, convergence was

Copyright © 2000 John Wiley & Sons, Ltd.

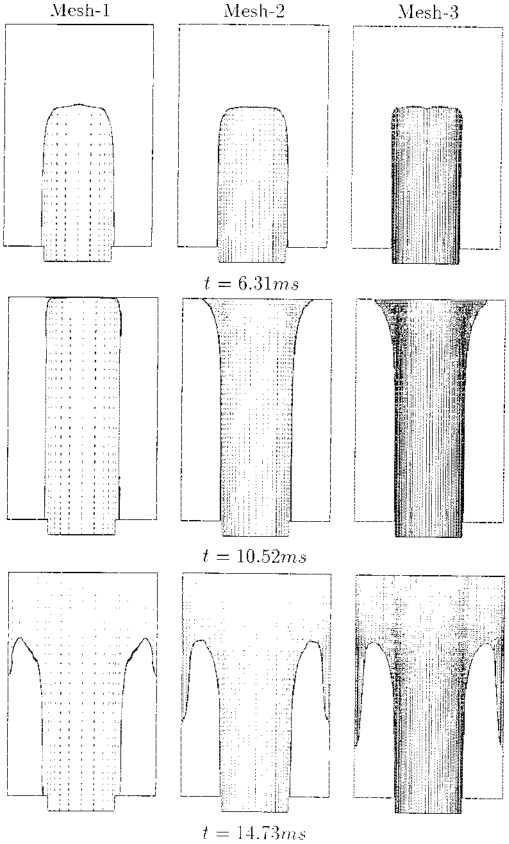

Figure 2. Filling of a plate: comparison of the numerical predictions for different meshes.

achieved when the relative correction on a global iterate was less than 10^{-6} for all variables. In most cases, three global iterations were sufficient to achieve the required tolerance. Sub-iterations on the non-linear systems on $\mathbf{u}$, k, and ϵ were performed until the relative error and the L_2 norms of the residuals were less than 10^{-6}. The front-tracking equation is linear and therefore two sub-iterations are enough to reduce the norm of the residual to 10^{-12}.

Simulations were performed with both the one-equation model and the k–ϵ turbulence model. The inlet turbulence level was set at 1 per cent. In order to estimate the cost associated to the use of turbulence modeling, computations were also performed for the laminar case with a constant eddy viscosity ten times higher than the laminar viscosity. For the laminar case, the turbulent law of the wall was still used, with a constant dimensionless distance to the wall $y^+ = 30$. All computations were performed in parallel on an Origin 2000 using four processors MIPS R10000 at 195 MHz. The mesh used for this application contains 10319 nodes and 46455 linear elements. The storage of the data structures and linear systems needed 9 Mb on

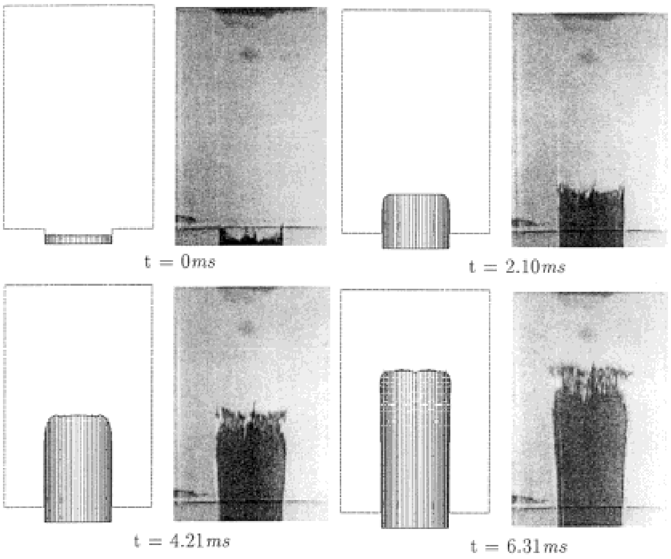

Figure 3. Filling of a plate: comparison of the numerical prediction with the experiment, from $t = 0$ to $t = 6.31$ ms (experimental results from Reference [25] courtesy of Schmid).

each processor. Computations take 17:20 h for the laminar case, 33:40 h with the one-equation model, and 52:10 h for the k–ϵ model. It shows that the one-equation model solution takes twice the time of the laminar computation, and that the k–ϵ model needs almost three times more computational time than the laminar solution.

The extrema of the turbulence variables are summarized in Table III. The maximum values are obtained near the gate region, while the minimum values are recovered on the lower-right end of the cavity. There are large variations of the momentum diffusion caused by turbulence fluctuations. A constant eddy viscosity model cannot account for those variations. The solution also depends on the implementation of the slip condition close to solid walls. Without turbulence modeling, the wall shear stress has to be considered from simplified assumptions. The shear stress may depend on the velocity, as for the present laminar approach, but it cannot lie on the turbulence level as turbulence variables are not computed. Because the wall shear stress determines the pressure drop, a constant eddy viscosity model will be inappropriate for cavities having long, thin sections. The heat transfer is even more sensitive and the temperature solution largely depends on the accuracy of the heat diffusion. Using a constant eddy thermal diffusivity for the viscosity will affect the temperature distribution. Consider the case of regions having low velocities and therefore low turbulence levels, as for the lower-right side of the cavity. In this region, turbulence models provide a turbulent viscosity 30–60 times lower than the laminar viscosity. An enhanced viscosity and thermal diffusivity solution will largely overestimate the heat diffusion in such regions. For real life applications, for which that may be unacceptable, turbulence modeling has to be incorporated into the solution algorithm.

Copyright © 2000 John Wiley & Sons, Ltd.

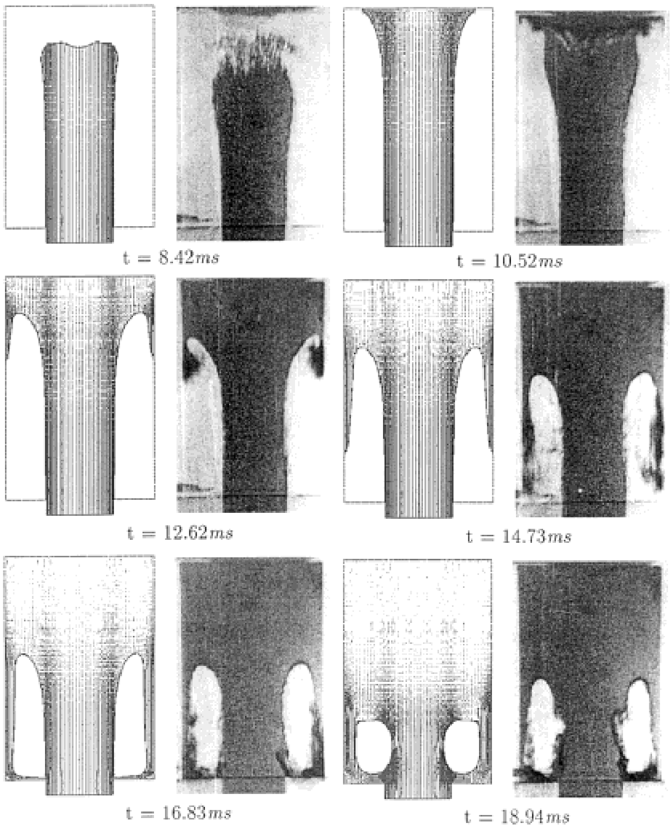

Figure 4. Filling of a plate: comparison of the numerical prediction with the experiment, from $t = 8.42$ to $t = 18.94$ ms (experimental results from Reference [25] courtesy of Schmid).

Table II. Material properties for filling problem.

Region	p (kg m^{-3})	μ (kg (m s)$^{-1}$)
Filling fluid	1124	4.66×10^{-3}
Air	1.17	1.98×10^{-5}

Figure 5 illustrates the flow front progression when the computations were performed with the one-equation model. The sequence of the filling stages for the $k-\epsilon$ solution are shown in Figure 6. The fluid accelerates in the inlet channel and passes through a gate having 0.125 dimensionless width (note that the reference length is equal to the inlet width). After the gate, the fluid hits the front wall and part of the fluid turns to the bottom and part of it flows over the horizontal plane. The two jets produce two strong recirculation regions. Once the bottom

Copyright © 2000 John Wiley & Sons, Ltd.

Table III. Variation of turbulence variables for the gravity filling (min/max).

Variable	k model	k–ϵ model
k (m^2 s^{-2})	$8.5\times10^{-6}/0.18$	$5.0\times10^{-7}/0.03$
ϵ (m^2 s^{-3})	$6.3\times10^{-7}/26.3$	$5.4\times10^{-7}/8.36$
μ (kg (m s)$^{-1}$)	$1.4\times10^{-4}/0.63$	$7.1\times10^{-5}/1.7\times10^{-2}$

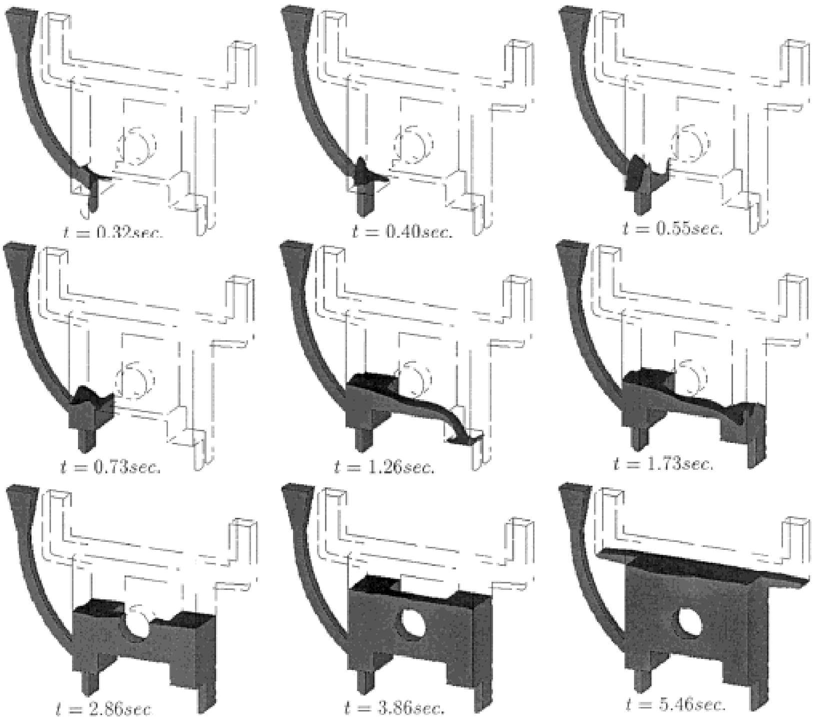

Figure 5. Mold-filling problem: flow front progression for the one-equation model.

left part of the cavity is filled (near section A in Figure 7), the recirculation produces a jetting flow along the vertical wall, especially for the $k-\epsilon$ solution. Then, the fluid flows over the horizontal plane and a jet is formed over the step at section G (see the solutions at $t = 1.26$ s). Once the bottom of the cavity is entirely filled, the interface becomes almost horizontal as expected for the filling in presence of gravity forces. As one can see, the interface is smooth indicating that the level set approach performs well. The results obtained with the $k-\epsilon$ model are comparable with those obtained with the one-equation model. However, the one-equation model introduces a higher eddy viscosity resulting in more viscous solutions.

Copyright © 2000 John Wiley & Sons, Ltd.

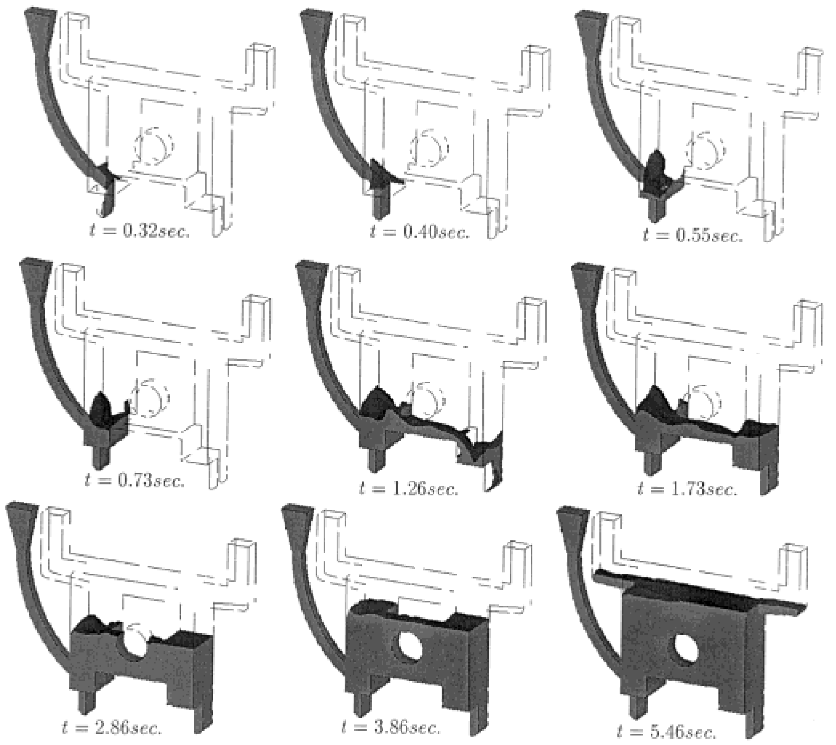

Figure 6. Mold-filling problem: flow front progression for the k–ϵ model.

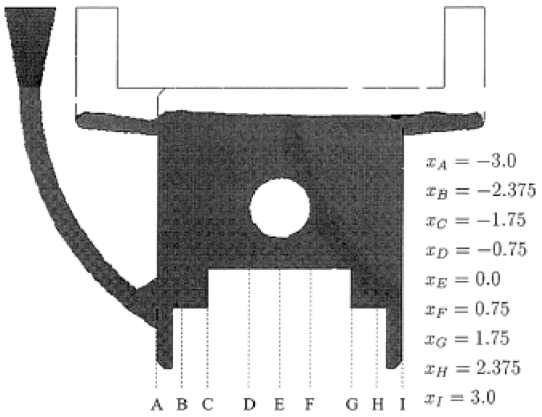

Figure 7. Mold-filling problem: location of the control stations in the experiment of McLeod [26].

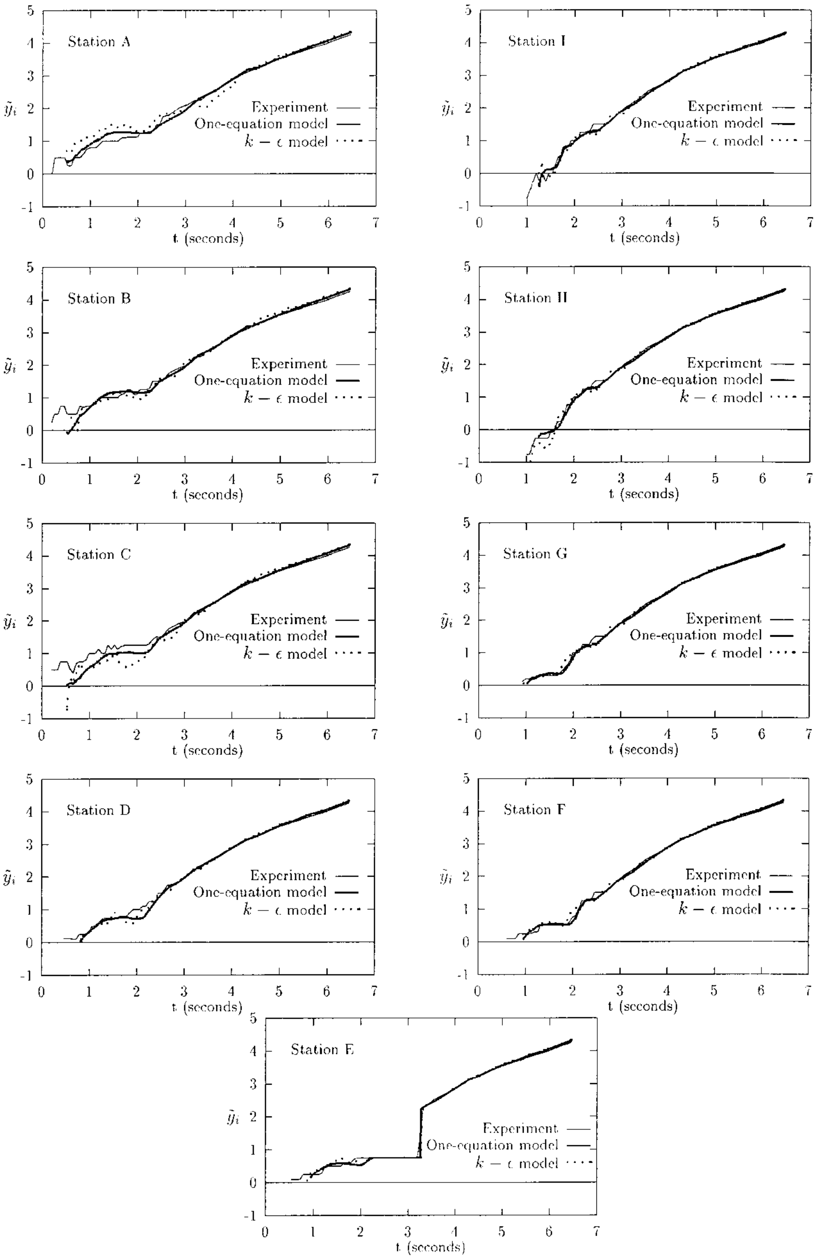

Figure 8. History of the free surface elevation at different control stations.

Experimental data for the free surface elevation is available for nine control stations as illustrated in Figure 7. Numerical predictions are compared with the experiment in Figures 8–10. Dimensionless co-ordinates $\tilde{x}$ and $\tilde{y}_i$ are computed as $\tilde{x} = x/L_0$, $\tilde{y}_i = y_i/L_0$. Subscript i denotes the free surface. Figure 8 presents the history of the free surface position for each control station. Good agreement with the experiment is observed. The agreement improves when moving from left to right (from station A to station I). This is because the flow behind the gate (near the stations A, B, and C) on the first part of the simulation is dominated by

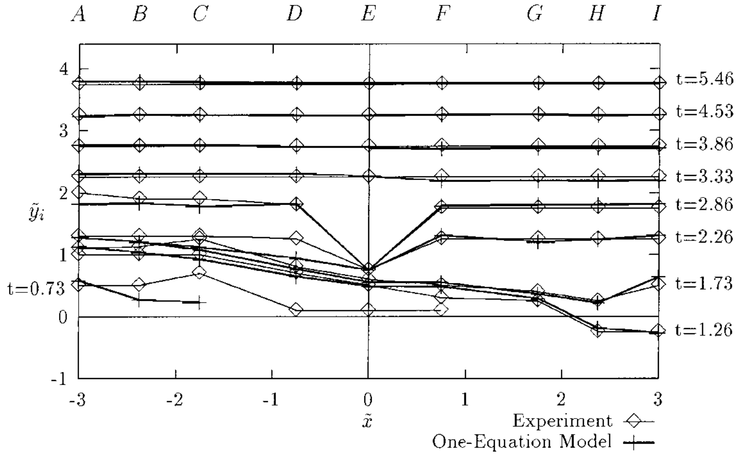

Figure 9. Position of the free surface: one-equation model compared with experiment.

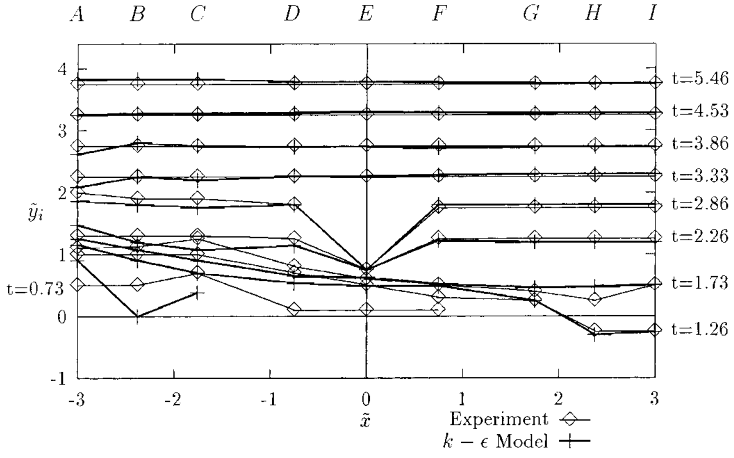

Figure 10. Position of the free surface: k–ϵ model compared with experiment.

Copyright © 2000 John Wiley & Sons, Ltd.

convection and the free surface elevation depends strongly on the depth location. On the second part of the simulation ($t > 3$ s), the agreement is excellent for all locations. The free surface contours at different times are plotted in Figures 9 and 10. The one-equation model results in closer to experiment solutions. However, the computations were done on a relatively coarse mesh. The somewhat better predictions of the one-equation model may be the result of a greater eddy viscosity, which acts like a damping mechanism on the free surface movement.

7. CONCLUSIONS

This paper has presented a methodology for solving transient three-dimensional turbulent flows for filling processes. A change of dependent variables that guarantees positivity of the turbulence variables in one- and two-equation turbulence models was presented. The procedure was applied to a simple one-equation turbulence model and to the $k-\epsilon$ two-equation model. The change of dependent variables results in a robust finite element algorithm capable of solving complex three-dimensional applications.

The finite element solution procedure solves in a partly segregated manner the momentum–continuity, turbulence, and front-tracking equations. This results in a robust solution algorithm applicable to large-scale three-dimensional problems. Applications have shown that the present procedure leads to reliable prediction of turbulent mold-filling problems. Solution for the one-equation model is more robust and cost effective than the one from the $k-\epsilon$ model. Such a simple turbulence model may be a good choice when large and demanding industrial applications are considered.

REFERENCES

1. Brooks AN, Hughes TJR. Streamline upwind/Petrov–Galerkin formulations for convective-dominated flows with particular emphasis on the incompressible Navier–Stokes equations. *Computer Methods in Applied Mechanics and Engineering* 1982; **32**: 199–259.
2. Hughes TJR, Franca LP, Balestra M. A new finite element formulation for computational fluid dynamics: V. Circumventing the Babuška–Brezzi condition: a stable Petrov–Galerkin formulation of the Stokes problem accommodating equal-order interpolations. *Computer Methods in Applied Mechanics and Engineering* 1986; **59**: 85–99.
3. Hughes TJR, Franca LP, Hulbert GM. A new finite element formulation for computational fluid dynamics: VII. The Galerkin–least-squares method for advective–diffusive equations. *Computer Methods in Applied Mechanics and Engineering* 1989; **73**: 173–189.
4. Ilinca F, Hétu J-F, Audet M, Bramley R. Simulation of 3D mold-filling and solidification processes on distributed memory parallel architectures. In *ASME Winter Annual Meeting. Proceedings of the Fluids Engineering Division*, Dallas, TX, vol. 244, Narain A, Kandlikar SG, Rohatgi US, Morrow TB, *et al.* (eds). ASME: Fairfield, NJ, 1997; 477–484.
5. Nichols RH. Development and validation of a two-equations turbulence model with wall functions for compressible flow. In *14th AIAA Applied Aerodynamics Conference*, New Orleans, LA. AIAA Paper 96-2385, 1996.
6. Suhs NE, Suhs RH, Nichols RH, Denny AG. Unsteady viscous flow computations using a two-equations turbulence model with wall functions for compressible flow. In *14th AIAA Applied Aerodynamics Conference*, New Orleans, LA. AIAA Paper 96-2430-CP, 1996.
7. Schonfeld T, Colin O, Rudgyard M. Parallel implementation of a $k-\epsilon$ turbulence model with wall functions for unstructured grids. In *27th AIAA Fluid Dynamics Conference*, New Orleans, LA. AIAA Paper 96-2061, 1996.
8. Ilinca F. Méthodes d'éléments finis adaptatives pour les écoulements turbulents. PhD thesis, École Polytechnique of Montréal, 1996.

Copyright © 2000 John Wiley & Sons, Ltd.

9. Ilinca F, Pelletier D. Positivity preservation and adaptive solution for the k–ϵ model of turbulence. *AIAA Journal* 1998; **36**(1): 44–50.
10. Ilinca F, Hétu J-F, Pelletier D. A unified finite element algorithm for two-equation models of turbulence. *Computers and Fluids* 1998; **27**(3): 291–310.
11. Launder BE, Spalding DB. *Mathematical Models of Turbulence* (6th edn). Academic Press: London, 1972.
12. Zienkiewicz OC, Sai BVKS, Morgan K, Codina R. Split, characteristic based semi-implict algorithm for laminar/turbulent incompressible flows. *International Journal for Numerical Methods in Fluids* 1996; **23**: 787–809.
13. Engelman MS, Sani RL, Gresho PM. The implementation of normal and/or tangential boundary conditions in finite element codes for incompressible fluid flow. *International Journal for Numerical Methods in Fluids* 1982; **2**: 225–238.
14. Gao D, Dhatt G, Belanger J, Cheikh AB. A finite element simulation of metal flow in molds. In *Numerical Methods in Thermal Problems*, vol. VI, Lewis RW, Morgan K (eds). Pineridge Press: Swansea, UK, 1989; 12.
15. Sussman M, Smereka P, Osher S. A level set approach for computing solutions to incompressible two-phase flow. *Journal of Computational Physics* 1994; **114**: 146–159.
16. Hétu J-F, Ilinca F. 3D GLS finite element formulation applied to mold-filling and solidification processes. In *Numerical Methods for Thermal Problems*, vol. X, Lewis RW, Cross JT (eds). Pineridge Press: Swansea, UK, 1997; 93–99.
17. Franca LP, Frey SL. Stabilized finite element methods: II. The incompressible Navier–Stokes equations. *Computer Methods in Applied Mechanics and Engineering* 1992; **99**(2–3): 209–233.
18. Tezduyar TE, Shih R, Mittal S, Ray SE. Incompressible flow using stabilized bilinear and linear equal-order-interpolation velocity–pressure elements. Research Report UMSI 90/165, University of Minnesota/Supercomputer Institute, Minneapolis, 1990.
19. Tezduyar TE, Aliabadi SK, Behr M, Mittal S. Massively parallel finite element simulation of compressible and incompressible flows. Research Report 94-013, Army High Performance Computing Research Center, Minneapolis, MN, 1994.
20. Ilinca F, Hétu J-F, Pelletier D. On stabilized finite element formulations for incompressible flows. In *13th AIAA Computational Fluid Dynamics Conference*, Snowmass, CO. AIAA Paper 97-1863, 1997.
21. Pelletier D, Ilinca F. Adaptive remeshing for the k–ϵ model of turbulence. *AIAA Journal* 1997; **35**(4): 640–646.
22. Saad Y. *Iterative Methods for Sparse Linear Systems* (1st edn). PWS Publishing Company: Boston, MA, 1996.
23. der Vorst HV. Bi-CGSTAB: a fast and smoothly converging variant of Bi-CG for the solution of non-symmetric linear systems. *SIAM Journal of Scientific and Statistical Computing* 1992; **13**: 631–644.
24. Schmid M, Klein F. Fluid flow in die cavities-experimental and numerical simulation. In *NADCA 18th International Die Casting Congress and Exposition*, Indianapolis, IN. Paper No. I-T95-034, NADCA (North American Die Casting Association), Rosemont, IL (ed.), 1995; 93–99.
25. Schmid M. Einfluß der wandreibung auf das füllverhalten dünner platten. In *17th Aalener Gießereisymposium*, 1996.
26. McLeod C. Modeling of aluminium gravity casting with water/glycerine solutions. Technical Report, Industrial Materials Institute, National Research Council Canada, 28 August, 1996.

Copyright © 2000 John Wiley & Sons, Ltd.